Materials Horizons

ROYAL SOCIETY OF CHEMISTRY

COMMUNICATION

View Article Online
View Journal

Cite this: DOI: 10.1039/d6mh00166a

Received 28th January 2026,
Accepted 11th April 2026

DOI: 10.1039/d6mh00166a

rsc.li/materials-horizons

Intrinsic mechanics of 3D-printed porous polymer-derived ceramic metamaterials

Youjian Li,[a] Vahid Karamzadeh,[b] Hamidreza Yazdani Sarvestani,[b] Hossein Mofatteh,[a] Zhengshu Yan,[ac] Ehsan Estakhrianhaghighi,[a] Michael Jakubinek,[d] Behnam Ashrafi,[b] Javad Gholipour*[b] and Abdolhamid Akbarzadeh*[ac]

Mechanical characterization of additively-manufactured polymer-derived ceramics (PDCs) remains challenging due to pyrolysis-induced porosity, flaws, and internal voids that bias conventional property measurements and mask the intrinsic bulk stiffness required for predictive metamaterial design. In this study, we introduce a hybrid experimental–numerical strategy to extract the intrinsic bulk Young's modulus of porous 3D-printed PDCs independent of their internal void structure. Hollow cylindrical specimens with systematically varied wall thicknesses are fabricated using liquid crystal display (LCD) printing and converted to silicon oxycarbide (SiOC)-based ceramics through pyrolysis. Micro–computed tomography (micro-CT) is used to capture the actual pore architecture, and a pixel-based reconstruction pipeline converts segmented micro-CT data into cubic-element finite element (FE) meshes. Compression tests provide experimental structural stiffness, while compression simulations of the same reconstructed geometries are performed using an assumed bulk Young's modulus. By leveraging geometrically identical models in experiments and simulations, the intrinsic bulk Young's modulus of 3D-printed PDCs is obtained from the stiffness ratio as 1.9 ± 0.1 GPa across specimens with different porosities. To determine the normalized modulus of the porous material, homogenization analyses are conducted on porous representative volume elements, establishing a strong relationship between normalized modulus and porosity. Finally, strut-based ceramic lattice structures are fabricated and tested, and two predictive FE approaches are demonstrated: a detailed FE approach based on micro-CT-reconstructed lattices and a computationally efficient FE–homogenization method using solid lattice geometries with porosity-informed effective properties. The developed hybrid experimental–numerical framework enables a robust extraction of bulk mechanical properties for porous ceramics and supports efficient, scan-light evaluation of the performance of porous ceramic metamaterials.

New concepts

This work introduces a hybrid experimental–numerical paradigm to directly extract the intrinsic bulk Young's modulus of porous 3D-printed polymer-derived ceramics (PDCs), decoupling material properties from pyrolysis-induced porosity and internal defects. Conventional approaches, such as nanoindentation or bulk testing, yield architecture-biased or overestimated stiffness values and cannot resolve intrinsic ceramic behavior in porous systems. By integrating micro-computed tomography, pixel-resolved digital reconstruction, finite element simulations, and representative-volume-element homogenization with mechanical experiments, we establish architecture-independent mapping between porosity and normalized modulus, enabling predictive design of porous ceramic lattices. Beyond PDCs, this framework provides a generalizable pathway to disentangle intrinsic material behavior from structural architecture in additively manufactured porous materials, bridging material characterization with metamaterial design and enabling predictive and inverse engineering of next-generation lightweight, high-performance ceramic metamaterials.

Introduction

Ceramics are among the oldest engineered materials and continue to play a significant role in the modern world, attributed to their hardness, thermal resistance, and chemical stability. These characteristics make ceramics attractive candidates for a wide range of applications, including aerospace, biomedical, electronics, energy, and many other industries. Polymer-derived ceramics (PDCs) have emerged as a versatile class of ceramics owing to their simple processing methods, low processing costs, and shape flexibility, which allows fabrication of complex geometries.[2–5] In contrast to conventional powder-based ceramics, PDCs originate from a preceramic polymer (PCP), such as polysiloxane, polysilazane, polycarbosilane,

[a] Department of Bioresource Engineering, McGill University, Montreal, QC, H9X 3V9, Canada. E-mail: hamid.akbarzadeh@mcgill.ca
[b] Aerospace Manufacturing Technology Center, National Research Council Canada, Montreal, QC, H3T 2B2, Canada. E-mail: Javad.GholipourBaradari@cnrc-nrc.gc.ca
[c] Department of Mechanical Engineering, McGill University, Montreal, QC, H3A 0G4, Canada
[d] Division of Emerging Technologies, National Research Council Canada, Ottawa, ON, K1A 0R6, Canada

and borazine, containing Si–O, Si–N, Si–C, and/or B–N bonds.[6–8] PCPs are shaped using polymer processing methods, such as injection molding, extrusion, casting, and other techniques, followed by crosslinking or gelling, and are pyrolyzed in a protective atmosphere at elevated temperatures, typically above 1200 °C.[7,9–12] During pyrolysis, gaseous byproducts such as H_2 and CH_4 are released, converting the organic precursor into a fully inorganic ceramic. The evacuation of these gases can generate voids within the solid, resulting in a porous material.

Despite these processing advantages and multifunctional potential, the intrinsic brittleness of ceramics and the porosity introduced during pyrolysis pose significant challenges for the mechanical performance of PDCs. Ceramics are inherently hard yet brittle and exhibit limited fracture resistance because they cannot undergo sufficient plastic deformation to prevent crack propagation.[13,14] To some degree, the existence of porosity further decreases the mechanical performance of PDCs. Nevertheless, these voids also impart beneficial properties, including low density, high permeability, and low thermal conductivity (excellent thermal insulation), and make porous PDCs promising materials for lightweight structural components, porous bioimplants, sensors, and other applications.[7,15–20] However, accurately determining the bulk Young's modulus of porous PDCs remains challenging, which hinders their further development and optimization.[16] Young's modulus is one of the most fundamental mechanical properties. Considering PDC is brittle and can hardly present plastic deformation upon loading, its elastic behavior becomes essential in the prediction of the mechanical performance of all kinds of multifunctional architected PDCs. Nanoindentation, which requires only a small testing volume, is commonly used to measure elastic moduli of PDCs;[21,22] however, this technique primarily probes local dense regions and is not accounting for the influence of porosity.[23,24] Consequently, the measured modulus may significantly overestimate the effective bulk modulus at the macroscale. Samples fabricated by hot isostatic pressing are fully dense and suitable for mechanical characterization.[25] However, complicated architectures such as cellular lattices cannot be manufactured *via* this processing technique, and thus, it will be inaccurate to predict mechanical performance with the mechanical properties determined by this method. Therefore, developing reliable approaches to evaluate the bulk elastic modulus of porous PDCs is essential for fully exploiting the unique properties of these ceramic materials.

These limitations motivate the exploration of alternative design strategies that can compensate for material-level deficiencies while preserving the intrinsic advantages of PDCs. Metamaterials, as a category of artificially engineered materials, demonstrate unparalleled properties that natural materials hardly possess.[26] Their outstanding performance, including negative Poisson's ratio, bi-/multi-stability, shape reconfigurability, stimuli-responsiveness, and multiphysics properties, relies on structural design rather than only the intrinsic properties of their constitutive materials.[27–34] Among them, lattices, also referred to as architected cellular materials, are among the most common structures in metamaterials. Commonly categorized into three groups, strut-based,[35–37] plate-based,[38,39] and shell-based[1,19,28] geometries, these metamaterials offer low density combined with high stiffness and strength.[40] Fabricating lattice structures based on PDCs is therefore promising for integrating excellent mechanical, thermal, and chemical properties. However, traditional shaping processes lack fabrication precision and freedom required to produce intricate architectures of metamaterials. Consequently, advanced manufacturing methods are needed to completely exploit the potential of PDC-based metamaterials.

The recent rapid development of additive manufacturing (AM) technology has provided a viable solution to the production challenges associated with PDCs. This technology, also known as three-dimensional (3D) printing, utilizes a computer-aided design (CAD) to fabricate components out of polymers, resins, ceramics, hydrogels, and metals in a layer-by-layer manner.[2,8,41–46] In contrast to conventional subtractive manufacturing processes, AM follows a bottom-up approach analogous to nature, *i.e.*, constructing objects from digital models rather than removing materials from bulk solids.[47] This characteristic of AM not only contributes to the reduction of time and material costs but also breaks the barrier of fabricating lightweight and geometrically complex PDC-based metamaterials. Various AM methods are employed to pattern PDC, such as digital light processing (DLP), stereolithography (SLA), two-photon polymerization (2PP), direct ink writing (DIW), and binder jetting.[8,14,48–54] Among them, common vat photopolymerization methods (SLA and DLP) are particularly promising approaches due to their high dimensional accuracy and compatibility with a large group of photocurable resins.[1,4] In these methods, ultraviolet light initiates photopolymerization within successive layers of liquid resin, enabling precise control over complex structures and providing a competitive and effective strategy for architecting PDCs into metamaterials.

While prior studies have reported local (*e.g.*, nanoindentation) moduli for near-dense SiOC prints, those approaches do not capture the bulk stiffness of inherently porous pyrolyzed structures.[23,50] Our method directly recovers a porosity-independent bulk Young's modulus, providing a more relevant benchmark for mechanical metamaterial design. In this research, as depicted in Fig. 1, a commercially available SiOC resin is used as the precursor to pattern a printable PDC with an LCD printer, aiming to investigate the bulk Young's modulus of a porous PDC. Despite its slow curing kinetics and high viscosity, the resin exhibits high printability strait. Although the printed samples are soft and viscous prior to pyrolysis, the as-pyrolyzed samples are solidified and demonstrate excellent mechanical properties.[2] Hollow cylindrical specimens are designed and scanned by a micro-computed tomography (micro-CT) scanner before being tested in compression experiments. A pixel-based method is utilized to reconstruct the cylindrical specimens with cubic elements so that they can be analyzed in simulations. Similar strategies have been reported on the investigations of geometric defects induced by selective laser melting technology, although the primary defect to explore is the morphology and distribution of strut width

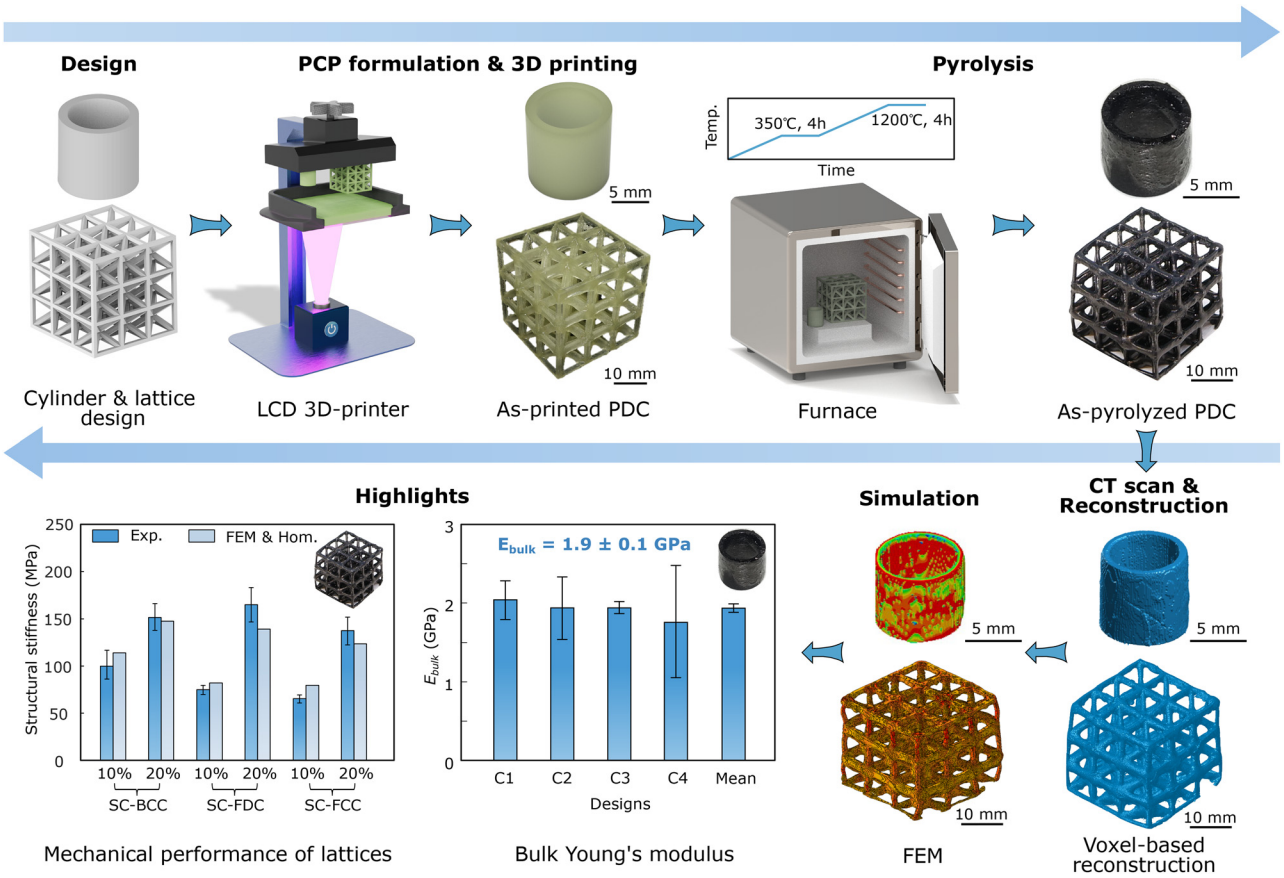

Fig. 1 A schematic workflow illustrates the integrated design, manufacturing, characterization, and modelling framework.

variance, and the reconstructed models are not feasible for direct analysis *via* finite element modelling (FEM) simulations.[55,56] Due to the identical geometries in the experiments and simulations, the bulk Young's modulus can be calculated regardless of the presence or absence of voids. Representative volume elements (RVEs) are created and analyzed using a homogenization method to obtain the normalized material properties of the porous PDC. Strut-based lattice structures are designed and tested. A numerical simulation method is proposed to predict how porous PDC-based lattices perform by employing solid structures and the bulk and normalized Young's modulus. The proposed approaches offer a promising pathway for investigating the bulk material properties of porous materials and predicting the performance of PDC-based metamaterials across a wide range of applications.

Experimental

Structural design

Cylindrical specimen designed for compression tests. Solid cylindrical specimens are commonly used in compression tests to characterize 3D-printed polymers and metals. However, this geometry is not suitable for 3D-printed ceramics, as porosity develops during pyrolysis, and thick specimens (*e.g.*, standard compression cylinders) tend to undergo significant distortion due to non-uniform shrinkage. To mitigate this effect, a hollow cylindrical geometry was designed, which reduces feature thickness and improves dimensional stability during pyrolysis, enabling reliable mechanical characterization of the resulting PDCs (Fig. 2a). The CAD model has an outer radius of 6.35 mm and a height of 12.7 mm. Empirically, the critical wall thickness of the SPR-684-based PCP, which is the material used in this research and will be introduced in the following section, is approximately 1 mm; below this value, the samples remain dense, whereas exceeding it results in significant porosity. Accordingly, samples with varying wall thicknesses were designed, leading to different relative densities ($\bar{\rho}$) of these samples, which are listed in Table S1 in Section S1 of the SI. These cylindrical specimens are designated as C1, C2, C3, and C4, where the letter "C" denotes the cylindrical geometry. These names are used instead of relative densities throughout the following sections to avoid confusion between the as-designed ($\bar{\rho}_d$) and as-fabricated relative densities ($\bar{\rho}_f$).

Cellular lattice design. Strut-based cellular structures slightly modified from traditional lattices were designed for investigation. In the conventional designs, unit cells are patterned periodically to form internal struts with widths twice as large as the external ones, which, empirically, causes significant porosity in the struts and intersectional nodes. Therefore, uniform struts are adopted throughout this study to avoid large

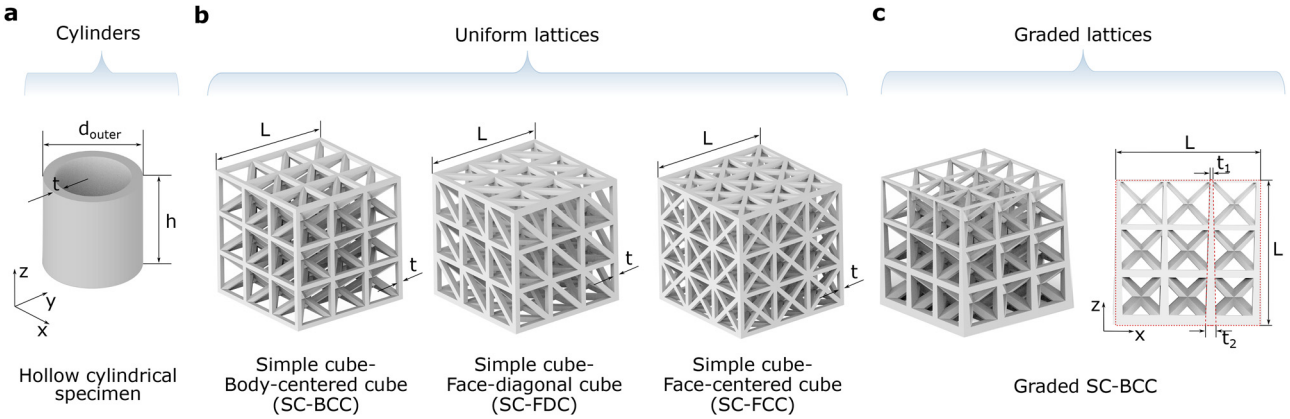

Fig. 2 As-designed models of (a) hollow cylindrical specimens, (b) SC-BCC, SC-FDC, and SC-FCC lattices, and (c) a graded SC-BCC lattice. Hollow cylinders have a uniform wall thickness throughout. SC-BCC, SC-FCC, and SC-FDC have different but uniform strut thicknesses, t. These uniform struts reduce the feature size compared to traditional lattices, whose strut widths are twice as large as those of the uniform lattices, and thus minimize unnecessary voids. The graded SC-BCC is a square frustum rather than a cube. The side views of its vertical and horizontal struts is an isosceles trapezoid with a top base, t_1, a bottom base, t_2, and a height, L, which are 0.6 mm, 2.0 mm, and 30 mm, respectively.

porosity. In this configuration, the total length of the multi-layer cellular structure, L, and the uniform strut width, t, determine the relative density of the as-designed hybrid simple cubic-body centered cubes (SC-BCC), hybrid simple cubic-face diagonal cubes (SC-FDC), and hybrid simple cubic-face centered cubes (SC-FCC) (Fig. 2b).[57,58] For all the samples, L is 40 mm, while t varies according to the relative density. Two relative densities, 10% and 20%, are considered in this study, and the number of layers is 3 for all samples. All the values are listed in Table S2 in the SI. Two small handles are designed on the bottom surface to assist in positioning the printing orientation after pyrolysis. It should be noted that lattices with 30% relative density are also designed; however, the as-fabricated samples were distorted and nearly bulk, so they were not used in the following research (Fig. S8 and Section S6 of the SI).

A graded SC-BCC with varying strut widths along the height direction was designed to explore the relationship between porosity and feature thickness (Fig. 2c). The total relative density is maintained at 20% throughout the structure, while the strut width changes uniformly from 0.6 mm at the top surface to 2.0 mm at the bottom surface. This graded variation includes horizontal, vertical, and inclined struts. The graded SC-BCC is a right square frustum rather than a cube, with side lengths of 29.3 mm and 30.7 mm for the top and bottom bases, respectively, such that the side length in the midsection is 30 mm, which is equal to its height.

Manufacturing

Resin preparation. A 3D-printable polymer-derived ceramic (PDC) formulation was employed using SPR-684, a silicon oxycarbide (SiOC) precursor from the polyramic® series (Starfire Systems, USA), which constitutes 69.3 wt% and serves as the preceramic polymer (PCP).[2] The formulation is further supplemented with SMS-992 (Gelest Inc., USA), a polythiol crosslinker, at 28 wt%; TPO-L (ethyl(2,4,6-trimethylbenzoyl) phenylphosphinate) at 0.5 wt% as a photoinitiator; 2-nitrophenyl phenyl sulfide (Tokyo Chemical Industry Co., Japan) at 0.1 wt% as a photoabsorber; and Pyrogallol (Molekula Americas LLC, USA) at 0.1 wt% as an inhibitor and stabilizer. These components were mixed using a Thinky ARE-310 planetary mixer (Thinky Inc., USA), starting at 2000 rpm for 5 minutes, followed by defoaming at 2200 rpm for 30 seconds, repeating as needed. In the following sections, the SiOC precursor SPR-684 will refer to the overall 3D-printable PDC formulation.

3D printing and pyrolysis. The prepared resin formulation was 3D-printed using an Elegoo liquid crystal display (LCD) printer (Elegoo, China) with a layer height of 50 μm. The build plate lifting speed was set to 20 mm min^{-1} for the first two seconds and 50 mm min^{-1} thereafter to protect both the printed models and the Teflon surface. The cylindrical specimens were printed along the height direction. Chitubox was used for slicing the CAD files and optimizing the printing parameters.

The pyrolysis protocol for the 3D-printed PDC was developed based on a previous study.[2] All pyrolysis steps were performed under a nitrogen purge (50 SCFH) in a furnace. Alumina tubes and plates were used to elevate the samples from the bottom of the furnace, promoting more uniform pyrolysis. Samples were heated from room temperature to 350 °C at a ramp rate of 1 °C min^{-1} and held at this temperature for 4 hours, followed by further heating to 1200 °C at the same rate, with a hold of another 4 hours. The slow heating rate allowed evolving gases to escape.[8] The first hold at 350 °C ensured the maximum polymerization, while the second phase ensured complete pyrolysis.

PDC characterization

Density measurement. An Ultrapyc 5000 gas pycnometer (Anton Paar Canada Inc., Canada) was employed to measure the density of 3D-printed PDCs. Argon gas was used to fill in the cell to add pressure to the samples.

Micro-CT scanning. A micro-CT specimen scanner, SkyScan 1172 (Bruker, Kontich, Belgium), was used to investigate the internal structure of 3D-printed PDCs. One sample from each cylindrical design was scanned. Image acquisition was performed with a voltage of 76 kV and a current of 131 μA, ensuring light transmission of 30–40%, with a 0.5 mm aluminum filter. The micro-CT images had a resolution of 1048 × 2000 pixels, with a voxel size of 9.89 μm. The exposure time was 885 ms per step, and the sample rotated by 0.4° per step over a total of 180°. During scanning, samples were enclosed in tightly fitting plastic wrap to prevent movement. NRecon (Bruker-micro-CT) was used for reconstruction, and CTan (Bruker-micro-CT) was used to analyze the geometric parameters. The densities of 3D-printed cylinders were calculated with the volumetric values obtained from 3D analysis and compared with measurements obtained using a gas pycnometer. A threshold value of 100–255 was applied to the images to segment the ceramic phase from the background.

Due to practical constraints, another micro-CT scanner, Zeiss Xradia Versa 520, was used to scan one SC-BCC and one graded SC-BCC specimen, as the previous equipment was no longer available. Image acquisition was performed at a voltage of 80 kV and a current of 87 μA, with an LE1 filter provided by Zeiss. The micro-CT images had a resolution of 1904 × 1882 pixels, with a pixel size of 24.97 μm for the SC-BCC and 19.65 μm for the graded SC-BCC specimens, respectively. The exposure time was 700 ms per step. Dragonfly (educational version) was used for reconstruction and porosity calculation.

Mechanical experimentation

Compression tests were performed on cylinders, SC-BCC, SC-FDC, and SC-FCC samples. The compression tests were conducted using an ADMET testing machine (ADMET, Norwood, MA, USA) and an MTESTQuattro testing control system equipped with a 20 kN load cell. The displacement rate was set to 5 mm min^{-1} to ensure a quasistatic compression condition at room temperature. A minimum of three specimens from each design were tested. A SONY DSC-RX100M4 camera was used to record videos of the experiments.

Numerical simulation

FEM & micro-CT. FEM was used to simulate the linear elastic deformation of the 3D-printed cylindrical samples under compression. Since the as-pyrolyzed samples were porous and exhibited irregular shapes distinct from the solid and regular CAD models, a meshed model replicating the actual sample was generated in MATLAB (MathWorks, Natick, MA, USA) using eight-node linear isoperimetric elements with reduced integration (C3D8R). In this process, micro-CT images were first imported, followed by grayscale conversion and binary segmentation. Three-dimensional coordinate grids were then created, and the nodes were numbered to form a structured mesh. The largest connected component was identified and retained, while other floating and isolated speckles were removed. More details can be found in Section S4 of the SI. Two parameters are employed to tune the resolution: the pixel number and the step number. The pixel number refers to the number of in-plane filled pixels, while the step number denotes a fixed interval at which the images are subsampled, with only one image selected per interval. For instance, when the step number equals one, all images are used for reconstruction, whereas only half of the images are selected when the step number equals two. Convergence tests were conducted on these parameters. The meshed model was then imported to Abaqus (Dassault Systèmes Simulia Corp., Rhode Island, USA) for the FEM simulation. One cylinder from each cylindrical design (C1–C4) and one SC-BCC with a relative density of 10% were scanned and analyzed *via* FEM with the above-mentioned pixel-based method. To distinguish simulations in this section from those described in the following sections, FEM based on micro-CT-reconstructed structures is referred to as FEM & Micro-CT.

The reconstructed cylindrical models were employed to determine the bulk Young's modulus of the PDC. A hypothetical bulk stiffness, E_{bs}, was assigned to the model, and Poisson's ratio was set to 0.11.[22,59] The bottom surface was fixed, and a displacement along the height direction was applied to the top surface. A load-displacement curve was obtained from the simulation result, and its linear slope, k_s, was acquired. Previously, the experimental load-displacement slope, k_e, was obtained from the compression tests. Since the geometries used in the simulations and the experiments were identical, the ratio of the true bulk Young's modulus of the ceramic material (E_b) to k_e equals the ratio of E_{bs} to k_s. Therefore, E_b can be calculated as:

$$E_b = \frac{E_{bs} \cdot k_e}{k_s} \quad (1)$$

The same reconstruction approach was repeated for SC-BCC lattices. FEM simulations were conducted *via* Abaqus with the assigned base material properties obtained from the previous paragraph, *i.e.*, E_b as the base Young's modulus. The bottom surface was fixed while a displacement was added to the top surface to simulate the initial elastic deformation. The structural stiffness was then calculated from the resulting force-displacement curve.

Homogenization analysis. Although FEM has been employed to investigate porous ceramics, this approach requires time-consuming and costly micro-CT scanning and may involve geometric features that are computationally prohibitive. Consequently, homogenization analysis based on RVEs provides an efficient alternative for determining the effective material properties of porous PDCs as building blocks and for predicting the mechanical behavior of PDC-based metamaterials.[60,61]

The RVE is constructed as a cubic domain containing randomly distributed ellipsoidal pores, which are more general and representative than spheroidal pores.[62,63] Each pore is defined by the lengths of its three principal semi-axes, a, b, and c; its center location $C(X, Y, Z)$; and two orientation angles, θ and ϕ, which describe its in-plane and out-of-plane rotations, respectively. The random sequential adsorption (RSA) technique, widely used for generating multiphase RVEs, was employed to populate the domain with pores.[64,65] In this approach, the cubic

unit cell is discretized into a 500 × 500 × 500 binary matrix, where voxels with a value of one represent the solid phase, and zeros represent pores. Pores are sequentially introduced until the target porosity is achieved. The ellipsoidal pore dimensions are determined from the mean pore sizes measured experimentally (Fig. S3 and Section S5 of the SI).[66] To avoid pore overlap, mitigate stress concentrations, and preserve isotropy and homogeneity, a minimum inter-pore distance equal to 1% of the minor semi-axis length is imposed.

Periodic boundary conditions (PBCs) are applied to the RVE unit cells because they provide accurate predictions of effective material properties.[64,65,67] For pores intersecting the boundaries of the cubic domain, geometric periodicity is enforced by removing the intersecting portion and reproducing it at the corresponding location on the opposite face. Periodic continuity is imposed on all vertices, edges, and faces of the RVE. The RVE models are generated in MATLAB and imported into Abaqus, where periodic ten-node quadratic tetrahedron elements (C3D10) are applied. A Python-based FEM script is then implemented in Abaqus to perform homogenization analyses and to compute the effective elastic modulus, Poisson's ratio, and shear modulus.[68]

At least five statistically independent RVEs are generated for each porosity level of 4%, 8%, 12%, 16%, and 20%. During homogenization, six independent loading cases—three uniaxial and three pure shear deformations—are applied in conjunction with PBCs. The equivalent macroscopic stress, $\bar{\sigma}$, and strain, $\bar{\varepsilon}$, are defined as the volume averages of the microscopic fields within the RVE:

$$\bar{\sigma}_{ij} = \frac{1}{V}\int_V \sigma_{ij}(m)\mathrm{d}V, \quad (i,j = 1,2,3, m \in V), \text{ and} \tag{2a}$$

$$\bar{\varepsilon}_{ij} = \frac{1}{V}\int_V \varepsilon_{ij}(m)\mathrm{d}V, \quad (i,j = 1,2,3, m \in V) \tag{2b}$$

where V denotes the volume of the RVE. The effective elastic constants of the equivalent homogeneous material is defined through the linear constitutive equations:

$$\bar{\sigma}_{ij} = \bar{C}_{ijkl}\bar{\varepsilon}_{kl} \tag{3}$$

where $\bar{C}_{ijkl}$ is the stiffness tensor of the equivalent homogeneous material. By solving the equilibrium solution for six independent loading cases, which consist of three pure axial and three pure shear deformation modes in the RVE, the components of $\bar{C}_{ijkl}$ are determined. The effective elastic properties of the 3D-printed PDC are then obtained from the compliance tensor, defined as the inverse of the stiffness tensor.

FEM & homogenization to predict mechanical properties of lattices. The porous as-fabricated SC-BCC lattices exhibit relatively irregular geometries, including uneven surfaces and bulging nodes, which makes it challenging to accurately predict their mechanical behavior using FEM. To address this limitation, an FEM-based numerical framework was developed to enable predictions based on idealized solid geometries combined with effective material properties obtained from homogenization analysis. The solid lattice geometries were identical to the as-designed models, while the overall lattice dimensions and strut widths were set to the mean values measured from the as-fabricated samples. Since the graded SC-BCC contains a wide range of strut width, it was scanned and used to establish a porosity-strut width relationship, which was then employed to predict the porosity of each lattice structure. The corresponding effective material properties were found according to the predicted porosities and assigned to the models. Representative examples can be found in Section S7 of the SI. Boundary conditions consisted of a fixed bottom surface and a prescribed displacement applied to the top surface. Finally, the structural stiffness of the 3D-printed PDC-based lattices was calculated from the resulting load-displacement curve. To distinguish this approach from the FEM & Micro-CT, the method described in this section is referred to as FEM & Homogenization.

Results and discussion

Manufacturing and material characterization

Micro-CT scanning is performed on 3D-printed cylindrical specimens, from which horizontal cross-sections are obtained (Fig. 3). Based on these reconstructions, the solid and void volumes are quantified, enabling the calculation of porosity, density, and relative density. Details of the calculation procedure are provided in Section S2 of the SI. Overall, the porosity of SPR-684 increases with increasing wall thickness. Cylinders C1 to C3 with lower as-designed relative densities of 20%, 30%, and 40% present relatively low porosities of 0.2%, 1.6%, and 5.4%, respectively. In contrast, C4, with an as-designed relative density of 50%, exhibits a much higher porosity of 41.4%, because the increased thickness hinders the release of gaseous byproducts generated during pyrolysis. As the gas diffusion path lengthens, gas escape becomes more difficult. When gas becomes trapped within the material, internal pressure rises, resulting in the formation of voids. This mechanism also causes geometric distortion, manifested as bulging surfaces in C4. Consequently, the overall shape, including solid and pore regions, expands considerably, leading to a significant reduction in the true relative density. By comparison, the difference between the as-designed and true relative densities remains small for the other samples.

Voids are distributed uniformly along the height in all samples except C3. In C3, the upper portion of the cylinder, accounting for approximately 75% of the total volume, exhibits a porosity of 2.4%, whereas the remaining 25% shows a much higher porosity of 13.5% (Fig. 3c). This nonuniform distribution is likely caused by thermal gradients in the furnace during pyrolysis or by insufficient mixing of the resin formulation prior to printing. The low-porosity upper region primarily contains flaws and small voids with sizes ranging from 0.02 to 0.15 mm, unlike the larger pores mostly ranging from 0.3 to 0.7 mm, observed in the lower region (Fig. S3 and Section S5 of the SI). In addition, the upper region displays a highly regular

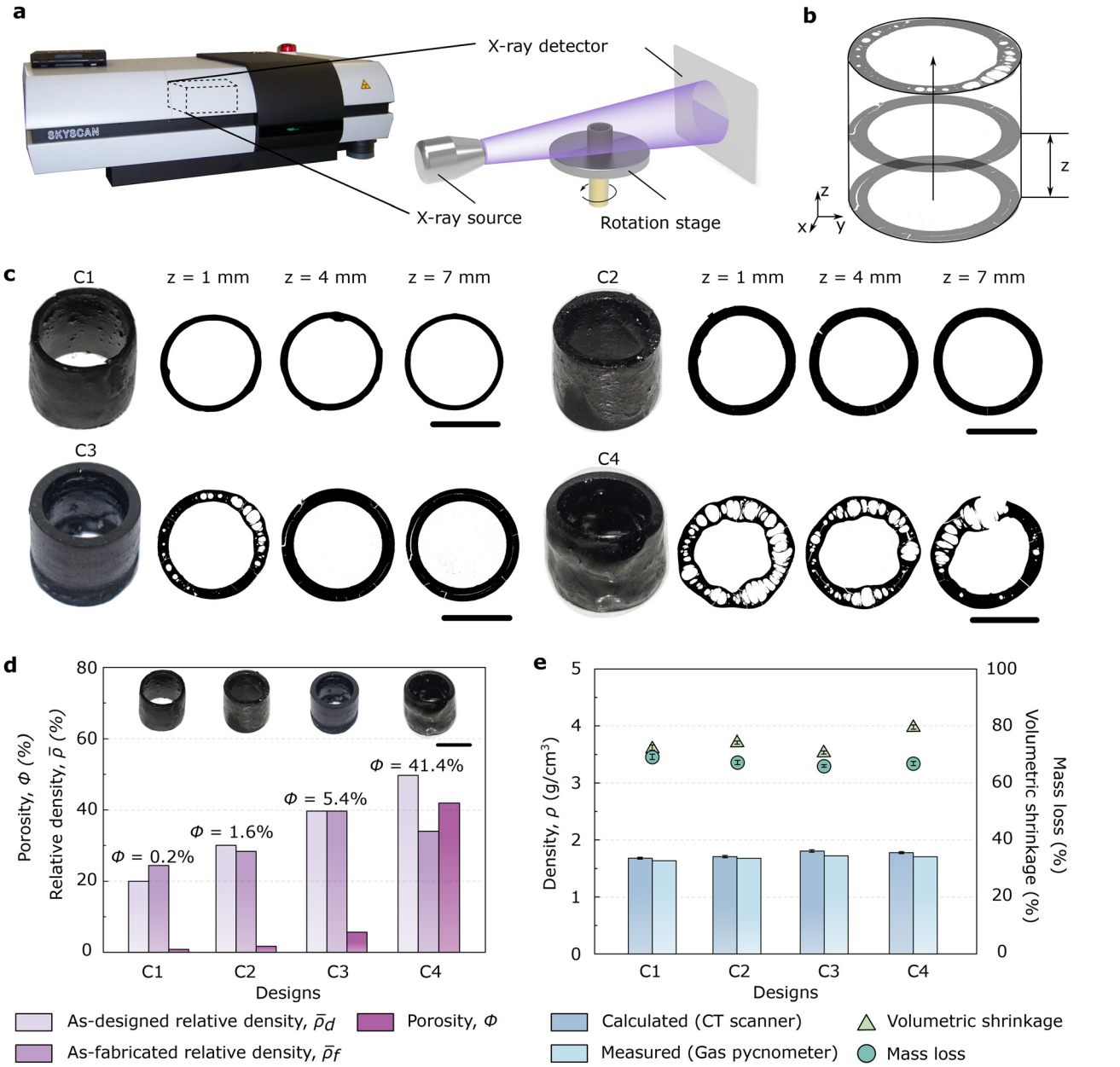

Fig. 3 (a) SkyScan 1172 micro-CT scanner and the schematic illustration of its principle. (b) Micro-CT scanner exports sliced cross-sectional images from bottom to top. The parameter, *z*, refers to the height from the bottom base. (c) Photos of the four as-fabricated cylinders (from C1 to C4) and three of the cross-sectional images with a height of 1 mm, 4 mm, and 7 mm, respectively. (d) The as-designed and as-fabricated relative densities and porosities of 3D-printed cylinders C1–C4. (e) The densities calculated from micro-CT and measured from a gas pycnometer, as well as the volumetric shrinkage and mass loss of C1–C4. Scale bar: 5 mm.

geometry and smooth surface, whereas the lower portion shows reduced geometric and dimensional accuracy.

For bulk density measurements of the 3D-printed PDC, a gas pycnometer utilizes differential pressure generated by argon gas and the volumetric displacement of the solid phase (Fig. 3e). Because argon gas cannot penetrate the ceramic walls to fill internal voids, the measured solid volume is overestimated, resulting in a lower apparent density. In contrast, densities calculated from micro-CT images reflect the true material state more accurately, as both open and closed pores are excluded when determining the solid volume. Nevertheless, the average bulk density of the 3D-printed PDC is 1.67 ± 0.04 g cm^{-3} as measured by gas pycnometer and 1.73 ± 0.06 g cm^{-3} as determined by micro-CT (Table S3 and Section S2 of the SI). These values align with previously published findings of SiOC-based PDCs.[1,2]

Mechanical characterization

After conducting compression tests on the cylindrical specimens, the bulk Young's modulus is calculated from the load-displacement

slope, k_e, the solid cross-sectional area that excludes voids, and the height of each sample. Fig. 4 presents representative load-displacement curves along with the corresponding fracture progression and mechanical properties. Overall, the bulk compressive modulus decreases with increasing porosity, although C2 ($\bar{\rho}_d$ = 30%) exhibits the highest stiffness. This trend and its associated deviation are mainly attributed to geometric imperfections, including the existing pores, flaws, and uneven bases of cylindrical specimens. Although volumetric shrinkage after pyrolysis is reasonably uniform, uneven or inclined top or bottom surfaces appear in nearly all the samples, with C2 being the least affected.

Upon initial loading, bulging regions in some samples are crushed into powders, while local cracks are generated in other regions originating from geometric defects and pre-existing microcracks. These defects lead to local or even global sudden and catastrophic brittle fracture. PDC is intrinsically brittle and exhibits limited toughening mechanisms, *e.g.*, the ability to resist crack propagation by enlarging the plastic deformation zone ahead of crack tips; the presence of voids, flaws, defects, and cracks further reduces the critical stress required to initiate failure.[13,69] After a short elastic regime, as shown in Fig. 4a–d, surface cracks form in C2 and rapidly cause fracture. The bulk

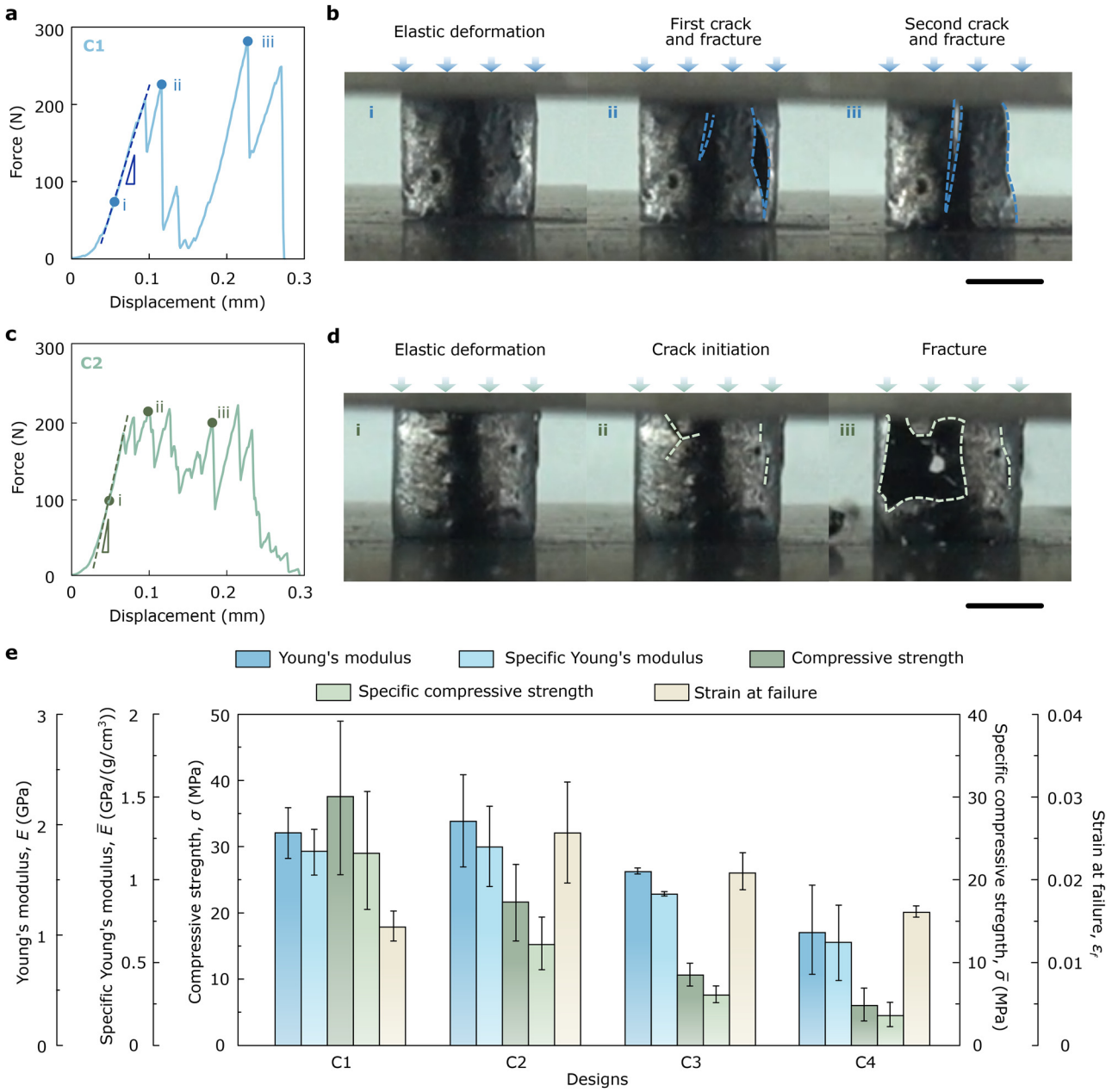

Fig. 4 (a) Displacement-load curves of C1 exhibits (b) elastic deformation, crack initiation and fractures. (c) Displacement-load curve of C2 displays (d) elastic deformation, crack initiation and growth and fracture. (e) Mechanical properties of 3D-printed cylindrical specimens, C1–C4, including Young's modulus, specific Young's modulus, compressive strength, specific compressive strength, and strain at failure. Scale bar: 5 mm.

stiffness measured for C1 ($\bar{\rho}_d$ = 20%) is comparable to, but slightly lower than, that of C2 (Fig. 4e and Table S7 and Section S3 of the SI). This arises because the uneven top surfaces of C1 break quickly, causing a major fracture across the specimen height and catastrophic structural damage, whereas fracture in C2 remains more localized and does not immediately affect the load-bearing capacity of the remaining structure (Fig. 4c). These mechanisms give rise to two characteristic load-displacement responses: one featuring multiple rises and peaks, and the other one showing a major rise followed by a wavy plateau. Nearly all the cylindrical specimens demonstrate one of these two types of curves.

Other than C1 and C2, C3 ($\bar{\rho}_d$ = 40%) and C4 ($\bar{\rho}_d$ = 50%) are particularly weakened by a combination of pores, flaws, and cracks. Although the effective solid cross-sectional areas of C3 and C4 exceed those of C1 and C2, the solid material is dispersed over a larger region (Tables S3–S6 and Section S2 of the SI). This solid distribution renders the overall structure akin to a random foam architecture full of flaws and cracks, resulting in lower compressive stiffness (Fig. 4e).

The methodology proposed in this study employs eqn (1) in combination with experimental and numerical results to determine the bulk Young's modulus. The calculated bulk stiffness, 1.9 ± 0.1 GPa, displays a low deviation and high uniformity across all specimens (Fig. 5). In the FEM simulations, only elastic deformation is considered, while plasticity and fracture behaviors are both neglected owing to the brittle nature of ceramics and the need to simplify the numerical models. Consequently, no force drop due to crack initiation or propagation is observed among all the geometries.

Although only solid areas are considered in calculating the experimental bulk Young's modulus, pre-existing cracks, and flaws weaken the material and reduce its stiffness. However, when the as-built geometry is exactly reproduced and the hypothetical elastic base material is assigned in FEM, the obtained bulk Young's modulus depends solely on the intrinsic material properties and is independent of porosity. Therefore, values obtained using the porosity-independent method (eqn (1)), which integrates both experiments and FEM, offer the most reliable determination of bulk Young's modulus. Mesh convergence analyses are also performed for the reconstructed models used in the FEM, and Fig. 5e shows that the selected mesh parameters fall within the converged regime.

When applying this methodology to evaluate the bulk Young's modulus, a key requirement is the use of identical geometries in both experiments and simulations (Fig. 5a–c). In the formulation, either k_e or k_b is expressed as a function of experimental loads and displacements and is independent of any geometric parameters; however, they are in fact governed by the structure and base material. Intuitively, structures with greater wall thickness and higher relative density should

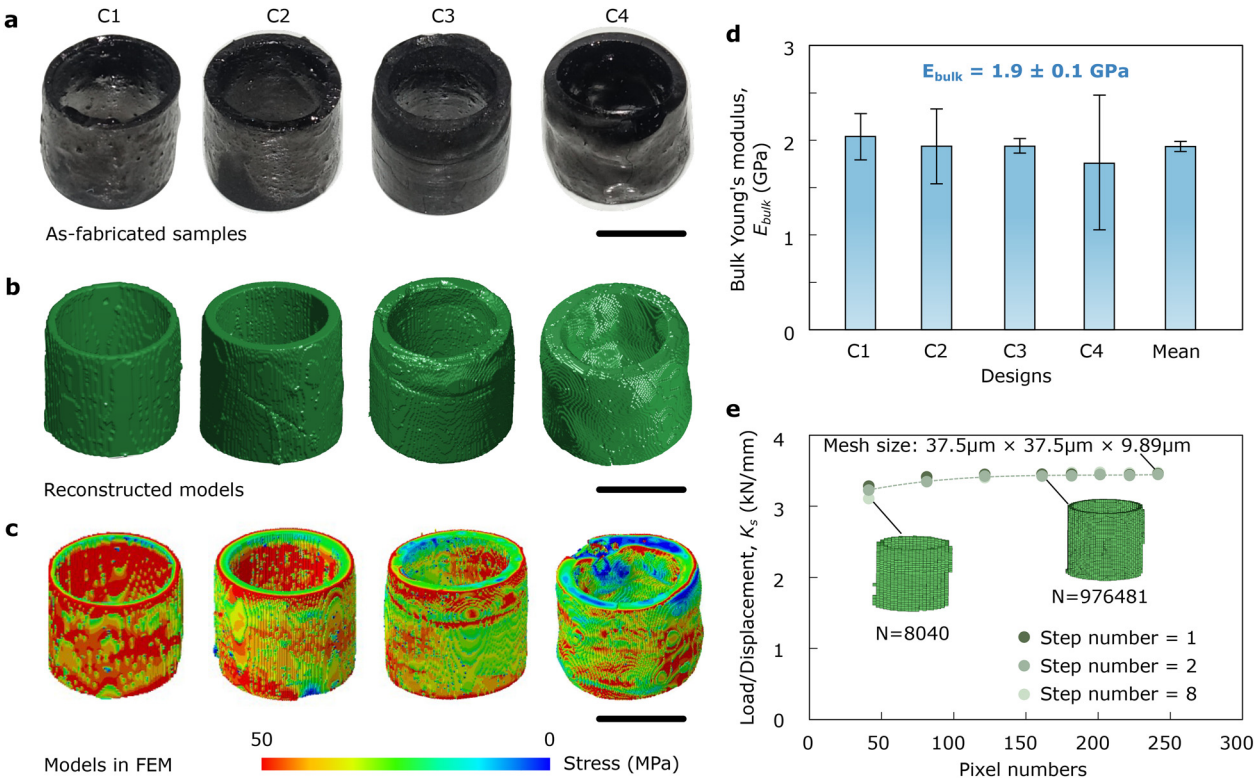

Fig. 5 (a) As-fabricated samples used for tests, (b) reconstructed models from micro-CT, and (c) meshed models simulated by FEM, from which (d) the bulk Young's modulus of PDC is calculated using the proposed porosity-independent methodology. The mean value is calculated from the results of C1–C4. (e) The effect of pixel numbers (*i.e.*, the in-plane pixel numbers that determine the in-plane resolution) and step numbers (*i.e.*, a fixed interval at which the images are subsampled, with only one image selected per interval) on the numerical results of reconstructed cylindrical specimens. *N* represents the total number of mesh elements. Scale bar: 5 mm.

possess superior mechanical properties, yet this rule does not hold for this PDC due to the existence of porosity. Experimentally, C1 and C2 achieve an optimal balance between solid areas and porosity and thus demonstrate the best mechanical performance.[70] However, this trend does not appear in the results obtained using the proposed methodology. Instead, the calculated bulk Young's modulus remains highly consistent across all specimens, demonstrating that the method effectively extracts intrinsic bulk stiffness irrespective of porosity. Furthermore, since the porosities of C1 and C2 (0.2% and 1.6%, respectively) are negligible, their experimentally measured bulk moduli—1.9 ± 0.2 GPa and 2.0 ± 0.4 GPa— are representative of the bulk ceramic (Section S3 of the SI). These values are in excellent agreement with the calculated bulk Young's modulus, thereby validating the proposed approach. These results are also consistent with previously reported values for additive-manufactured SiOC-based PDCs with similar compositions.[1,2]

Fig. 4e also depicts additional mechanical and specific mechanical properties among cylindrical specimens beyond the stiffness. Given the significant geometric and dimensional variations among cross-sections along the printing direction, using an average cross-sectional area to determine the compressive strength may lead to inaccurate stress estimation. In addition, failure is most likely to initiate at the smallest cross-section, where stress concentration is highest. Therefore, the compressive strength is defined as the maximum stress, calculated as the ratio of the maximum force to the minimum cross-sectional area. The maximum compressive strength decreases as the porosity increases, and the highest value is achieved by C1 at 37.6 ± 11.8 MPa (Fig. 4e and Table S7 and Section S3 of the SI). The load-displacement curve of C1 contains several linear stages (Fig. 4a and b). Each stage starts with a smooth rising curve and terminates with a dramatic drop, indicating that the structure withstands the load until crack initiation, followed by rapid crack propagation and catastrophic fracture along the sample height. Nevertheless, apart from the fracture region, the remaining portion of the sample continues to bear load until a larger force triggers the next fracture. For the other samples, a single major fracture happens and leads to complete structural failure, so their load-displacement curves do not exhibit multiple load drops. As a result, the strain at failure of C1 is smaller, while the highest value (2.6 ± 0.6%) is obtained from C2.

Homogenization and mechanical characterization of lattices

Homogenization analysis is performed on RVEs with different porosities. The RVE designs and the corresponding results are presented in Fig. 6. The normalized Young's modulus in the principal direction, E_{11}/E_{bulk}, decreases monotonically from 0.93 to 0.64 as the porosity increases from 4% to 20%. A regression analysis is conducted on these data, yielding a linear regression equation expressed as

$$y = -0.0668x + 0.9894 \quad (4)$$

where y denotes E_{11}/E_{bulk} and x represents porosity. The coefficient of determination (R-squared = 0.9979) indicates an excellent linear fit. The Poisson's ratio varies only slightly among the principal directions and across RVEs with different porosities, confirming a high degree of isotropy and validating the RVE design (Fig. S6 and Table S8 in Section S5 of the SI). The effect of mesh element size is also examined through convergence tests, with element size from 0.15 mm to 0.03 mm, and the results become convergent when the elements are smaller than 0.08 mm, as detailed in Section S5 of the SI.

Fig. 7 illustrates the as-fabricated samples and reconstructed models of one 3D-printed SC-BCC with a relative density of 10% and one graded SC-BCC. Like other as-fabricated lattices, these specimens turn black after pyrolysis, and the overall geometries deviate from the ideal as-designed structure. Along the printing direction, the SC-BCC cube resembles a square frustum, with a smaller top layer and a larger bottom layer. For graded SC-BCC, which should be similar to a cube, the difference between the top and bottom surfaces becomes more obvious. For both samples, bulges can be observed at the intersecting nodes and in the middle of the struts, where wavy shapes develop. Small local breakages are also observed at the corners, which is likely caused by damage incurred during the transportation of the brittle PDC samples. Another possible reason is that after printing, the preceramic part is too soft and sticky and thus prone to damage when removing the printed part from the build plate. This behavior is commonly seen in SC-FCC lattices (Fig. S7 and Section S6 of the SI), especially in structures with thin struts (less than 0.5 mm). It should also be noted that the vertical struts are generally thinner than the horizontal ones. This anisotropy might be induced by gravity during printing, which elongates the vertical struts while widening horizontal struts.

The micro-CT reconstructed model offers detailed insight into the internal structures of the lattice for further investigation (Fig. 7b). In Type-I cross-sectional images, taken in planes containing horizontal struts, pores are distributed throughout the structure, including within struts and at nodal junctions. This void distribution is consistent across layers, yielding an average porosity of 29.5%. Type-II and -III slices, located between Type-I layers, contain both vertical and inclined struts characteristic of the SC-BCC geometry. Similar to the intersections of horizontal struts, the body center, which is the central junction of inclined struts, demonstrates a high porosity due to localized material accumulation, corresponding to an increased effective feature thickness. The average porosity in Type-II and -III layers is 35.5%. However, the vertical struts exhibit a much lower average porosity of 6.8%, making them significantly denser than other structural components and explaining their comparatively thinner appearance. When vertical struts are excluded, the remaining regions exhibit an average porosity of 38.0%, comparable to that of Type-I layers. Overall, although the average porosity of the SC-BCC lattice with a relative density of 10% is 32.5%, the void distribution is highly nonuniform, with substantially lower porosity in the vertical struts than in the rest of the structure. A similar trend is noticed for graded SC-BCC, and its porosity distribution is shown in Section S7 of the SI.

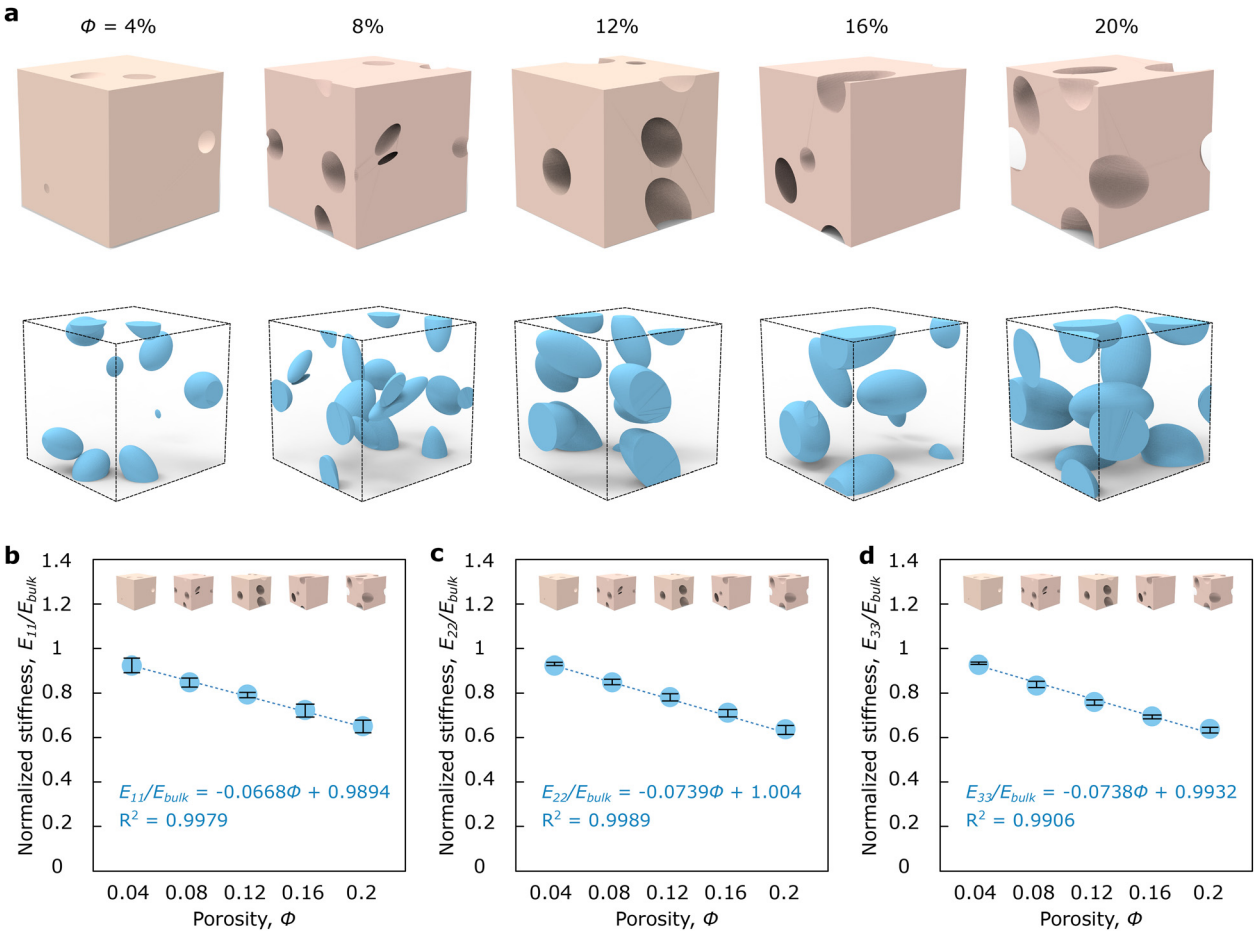

Fig. 6 (a) Porous RVE models corresponding to each porosity value used in homogenization analysis and the 3D models of their ellipsoidal pores. (b–d) The numerical values of normalized stiffness E_{11}/E_{bulk}, E_{22}/E_{bulk}, and E_{33}/E_{bulk}, respectively, and their relationships with porosity. Linear fitting curves are displayed, and the coefficients of determination (R^2) are 0.9979, 0.9989, and 0.9906, respectively.

Despite its effectiveness in revealing internal architectures, micro-CT scanning is costly and time-consuming, which limits its applicability for large sample sets. Consequently, this study proposes an FEM-based approach to predict the mechanical properties of lattice structures using a limited number of scans (Fig. 8). A solid SC-BCC model is designed for FEM to validate the experimental results and the FEM results derived from micro-CT-reconstructed models. For the PDC-based SC-BCC lattices with a relative density of 10%, the as-fabricated total length averages 25.4 ± 1.5 mm, and the effective strut width is 1.3 ± 0.2 mm. These values are used as the geometric inputs for the FEM models.

Four different material property assignment strategies are considered. Assignment-I treats the lattice as a homogeneous material with an overall porosity of 32.5%. Since the geometry is intact, the fact of porosity will be exhibited by multiplying the base PDC Young's modulus using the normalized stiffness of this porosity obtained from eqn (4), *i.e.*, 1.9 GPa × 0.47 = 0.9 GPa. Assignment-II partitions the lattice into two regions: layers containing horizontal struts with a porosity of 29.5% and the remaining regions with a porosity of 35.5%. Assignment-III further separates the vertical struts (6.8% porosity) from the Type-II layers, resulting in a remaining region with a porosity of 38.0%. Assignment-IV merges the Type-I, -II, and -III layers, excluding the vertical struts, into a single region with an average porosity of 34.8%. Using eqn (4), the equivalent Young's moduli of PDC corresponding to porosities of 6.8%, 29.5%, 34.8% 35.5%, and 38.0% are calculated as 1.8, 1.0, 0.82, 0.79, and 0.7 GPa, respectively, which are then assigned to the corresponding regions in the FEM models.

The load–displacement curves of the 3D-printed SC-BCC lattices with a relative density of 10% are obtained from compression tests, yielding an average Young's modulus of 104.2 ± 15.2 MPa (Fig. 8b and c). The mechanical properties of as-pyrolyzed lattice specimens are affected by the existence of voids, flaws, and cracks. Since PDC is a brittle material that possesses an extremely limited intrinsic toughening mechanism, plastic deformation is rarely observed during loading.[13] Thus, it is difficult for such a ceramic to prevent an existing crack from propagating through plastic zone development. In Fig. 8b, although the whole curve seems complicated and non-linear, it contains only short but steep elastic regions, accompanied by minor drops and fluctuations, prior to catastrophic collapse.

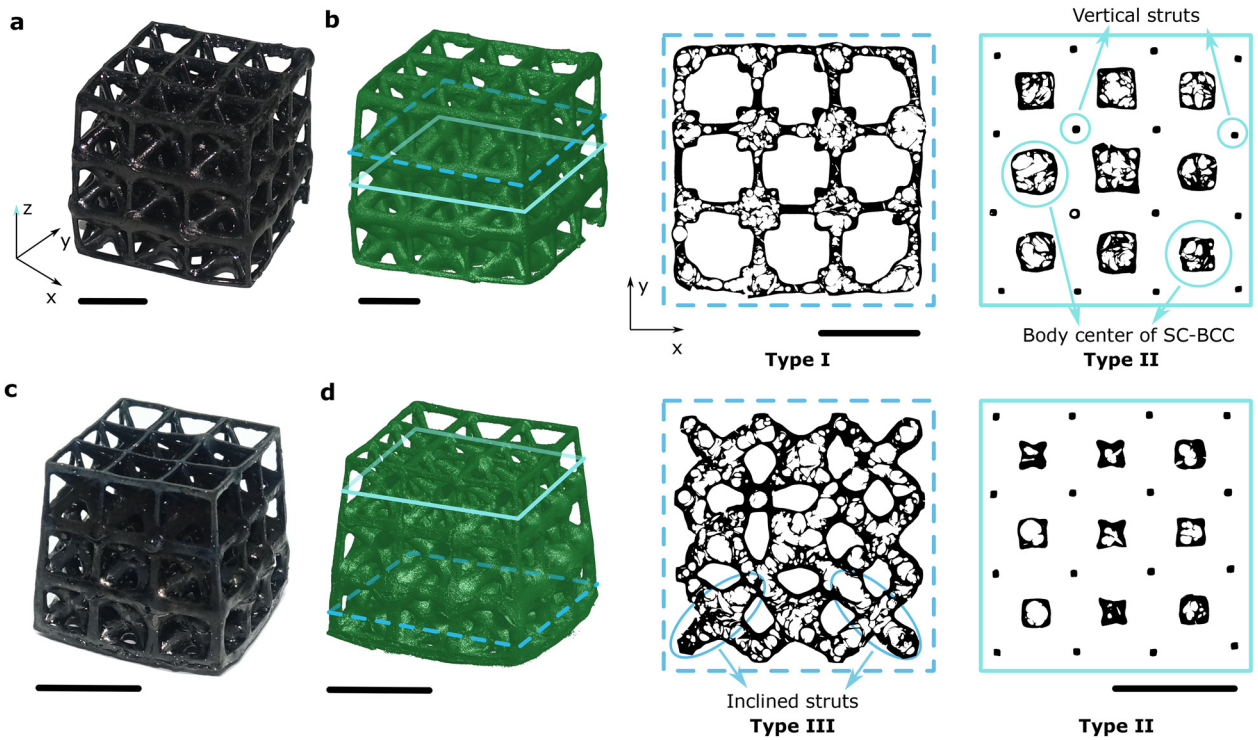

Fig. 7 (a) As-fabricated SC-BCC and (b) its reconstructed model along with two typical sliced cross-sectional images showing the horizontal struts (in blue square) and the body center and vertical struts (in grey square), respectively. (c) As-fabricated graded SC-BCC and (d) its reconstructed model along with two sliced images showing the inclined struts (in blue dashed square) and the vertical ones and body centers (in cyan solid square), respectively. Scale bar: 10 mm.

Bulging nodes are commonly observed on the top surfaces of the as-pyrolyzed samples. These features are the first to contact the compression platen and are easily crushed, causing the initial fluctuations observed in the load–displacement curves. Internally, pores are widely distributed throughout the lattice, while the surfaces contain numerous small flaws formed during gas evacuation in pyrolysis. As a result, even small cracks can propagate without arrest, linking pre-existing defects and leading to sudden catastrophic failure. For most SC-BCCs, SC-FDCs, and SC-FCCs, a fracture initially remains locally and damage porous and weak parts at the corner or on the top or bottom surfaces (Fig. S10 and Section S6 of the SI). Once an entire layer is fully destroyed, a global crack suddenly occurs vertically and breaks the sample into two parts. This crack usually happens in the middle of unit cells, which is probably attributed to the large porosity at the face- or body-centered regions, and simultaneously damage the vertical and inclined struts.

Good agreement is observed between the experimentally measured Young's modulus (104.2 ± 15.2 MPa) and the values calculated by FEM & Micro-CT and FEM & Homogenization, which are 98.6 MPa, and 112.5 MPa, respectively. Convergence tests are conducted to investigate the effects of spatial resolution in 3D directions on the pixel-based reconstructed model (Fig. S12 and Section S7 of the SI). Overall, higher resolution reconstructs a more accurate geometry but significantly increases computational cost. Since the reconstruction is based on two-dimensional micro-CT images with a fixed spacing, the out-of-plane (z-axis) resolution is inherently limited by the slice thickness. In contrast, the in-plane (x- and y-axis) resolution can, in principle, be refined further, subject to computational constraints, but it cannot exceed the intrinsic resolution of the micro-CT images. In the current simulations, the numerical model consists of approximately 9×10^7 cubic elements, where every other micro-CT image is selected to reconstruct, and 360 × 360 pixels are used in the in-plane directions, resulting in a final voxel resolution of 104.91 μm × 103.85 μm × 50.02 μm (Fig. S12 and Section S7, SI). The predicted structural stiffness closely matches the experimental value, further validating the previously determined bulk PDC properties. For the FEM & Homogenization approach, the fourth material assignment offers the most accurate and closest result to experiments and FEM & Micro-CT. This assignment explicitly distinguishes the vertical struts, which not only exhibit substantially different porosity compared to other structural components but also play a critical role in sustaining compressive loads, while remaining more computationally efficient than the third assignment strategy. Nevertheless, the idealized solid lattice models do not explicitly capture the porous and mechanically weak regions present in real samples, which are prone to early fracture and stiffness degradation subject to load. As a result, the FEM & Homogenization approach slightly overestimates the experimental stiffness. Overall, this method is validated by experimental and FEM & Micro-CT results

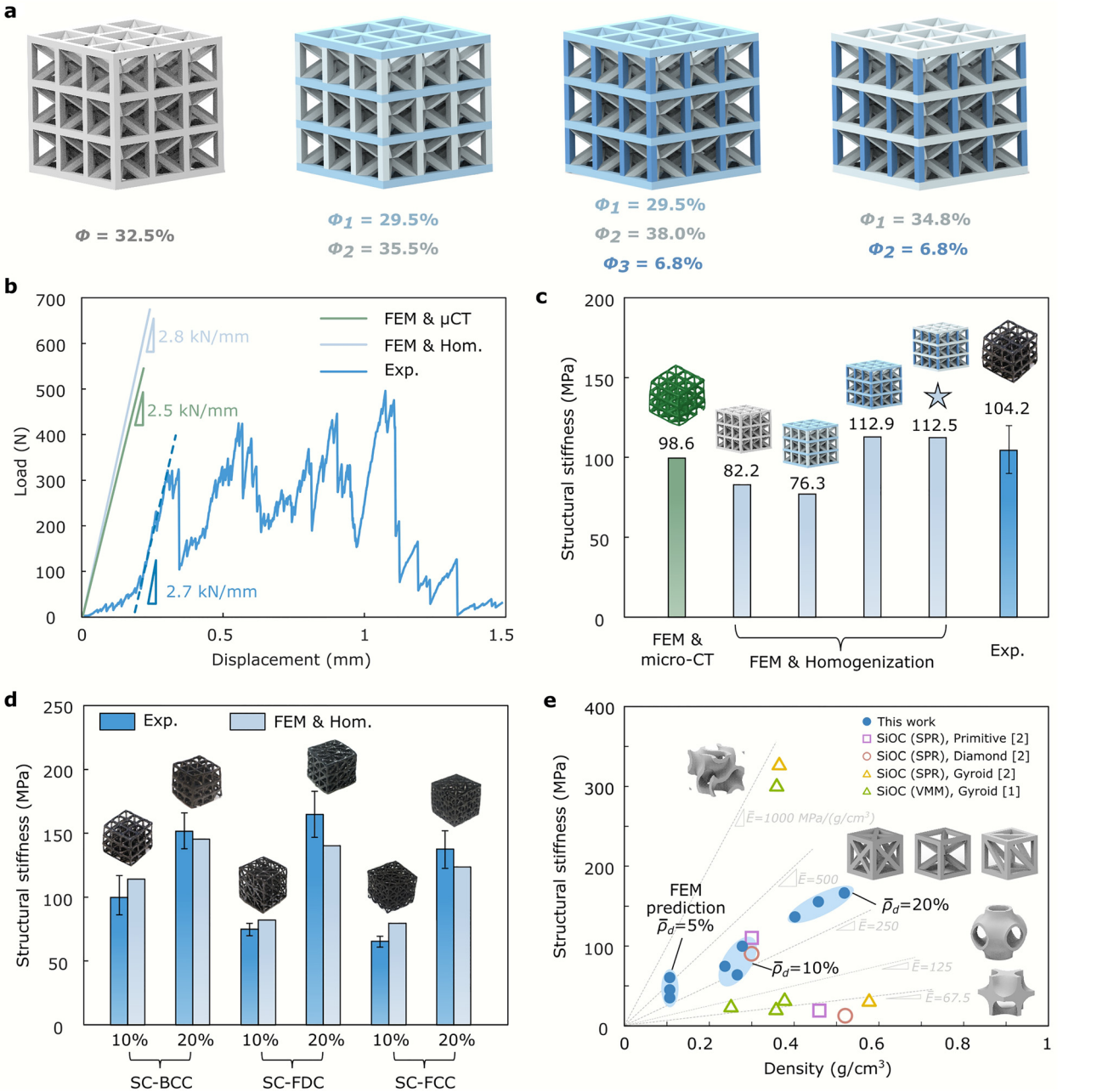

Fig. 8 (a) Four different material assignments in FEM that are applied to the scanned SC-BCC with a relative density of 10% based on the porosity distribution and homogenization results. (b) Load-displacement curve of compression experiments, FEM & Micro-CT, and FEM & Homogenization. (c) Young's modulus of BCC with a relative density of 10% from experiments, FEM & Micro-CT, and FEM & Homogenization with four material assignments. Assignment-IV, the material assignment denoted with a star provides the most accurate and closest result to the tests. (d) Experimental and computationally predicted Young's moduli of SC-BCCs, SC-FDCs, and SC-FCCs with relative densities of 10% and 20%, respectively, from compression tests and FEM & Homogenization. (e) A performance chart depicting how Young's modulus performs *versus* density in strut-based metamaterials made of 3D-printed SiOC-based PDC, compared to shell-based lattices reports.[1,2] The light blue shaded regions represent the sets of resulting data points obtained as the corresponding effective elastic moduli vary within a reasonable range. The light grey guidelines provide information of specific stiffness, which makes comparison among varied results easier. The slopes of these guidelines use MPa $(g\ cm^{-3})^{-1}$ as units.

and can be used to predict the mechanical performance of other lattices.

Fig. 8d presents the Young's modulus of SC-BCC, SC-FDC, and SC-FCC lattices with relative densities of 10% and 20%, as obtained from both experiments and FEM & Homogenization. Overall, the numerical predictions show good agreement with the experimental results. For lattices with a relative density of 10%, SC-BCC structures exhibit the highest stiffness and the greatest mass (mean value = 5.98 g). The stiffness of SC-FDCs is lower because these lattices are the lightest (mean value = 4.15 g),

which may be attributed to a less complicated architecture compared with the other two that allow complete removal of excessive resin. As shown in Fig. 8e, the specific stiffness of SC-FDC with a relative density of 10% is comparable to that of SC-BCC with the same relative density. For SC-FCCs, geometric defects—such as a fully missing bottom surface and big air bulges in the connecting nodes—contribute to the lowest elastic modulus. Increasing the relative density to 20% leads to a substantial increase in Young's modulus compared with the 10% counterparts, with SC-FDC lattices exhibiting the highest stiffness due to their least distorted geometry. SC-BCCs resemble a square frustum. Owing to the viscosity of the PCP resin, residual material that is not fully rinsed can become partially or fully cured, resulting in increased feature thickness and surface bulges in the as-pyrolyzed samples (Fig. S7 and S8 and Section S6 of the SI). SC-FCC lattices exhibit the most uneven surfaces, as voids tend to concentrate at face centers and at the intersection nodes of unit cells. Consequently, both SC-BCC and SC-FCC lattices show relatively lower rigidity. Moreover, because the effective Young's moduli assigned to the numerical geometries are calculated from the estimated porosities, the porosity values are then varied within a reasonable range, and additional FEM simulations were performed. The sets of resulting points are plotted as a light blue shaded region in Fig. 8e.

When predicting the performance of these porous lattices using FEM & Homogenization, it is observed that the numerical results are greater than the experimental ones for structures with a relative density of 10% but smaller for those with a relative density of 20%. These variances arise from differences in porosity and the equivalent stiffness assignment for each phase in FEM. Because only graded SC-BCC lattices are designed and scanned, the relationship between porosity and strut width derived from these samples serves as the sole reference for uniform SC-BCC, SC-FDC, and SC-FCC lattices. The geometric differences affect the pyrolysis performance and ultimately result in differences in the void distribution of each architecture. In addition, it is an estimation rather than an analytical equation that is obtained from the scanned graded SC-BCC; thus, errors are generated when assigning such an equivalent mechanical property to the simulation models. Such errors are inevitable unless micro-CT scanning is conducted on a broader set of samples, but the values are moderate after all. Overall, the discrepancies shown in Fig. 8d remain acceptable for design and optimization purposes and further validate the applicability of FEM & Homogenization for PDC-based lattice structures. This method is then subsequently utilized to predict SC-BCC, SC-FDC, and SC-FCC with a relative density of 5% (Fig. 8e), which demonstrates excellent mechanical efficiency, *i.e.*, a high stiffness-density ratio. This approach also shows strong potential to supplement experimental data and to facilitate the optimization of additively manufactured PDC-based metamaterials.

Conclusion

In this study, we fabricate PDCs *via* additive manufacturing and establish a robust framework to determine their intrinsic bulk Young's modulus despite inherent porosity. A hybrid experimental–computational approach combining hollow-cylinder compression tests, micro-CT scanning, pixel-based microarchitecture reconstruction, and FEM enables porosity-independent extraction of the bulk Young's modulus, 1.9 ± 0.1 GPa, validated across specimens with varying porosity. A homogenization approach based on RVE models is developed to quantify the relationship between porosity and effective stiffness, yielding a linear predictive model for the effective Young's modulus. Strut-based lattice ceramic metamaterials are designed and characterized, revealing printing-induced geometric anisotropy with thinner and stronger vertical struts, which are captured through coupled micro-CT-based FEM simulations and experiments. Building on these results, a combined FEM–homogenization framework is proposed to predict the mechanical response of PDC metamaterials using intact geometries and effective stiffness parameters, significantly reducing reliance on time-intensive micro-CT characterization. Overall, this work introduces a generalizable methodology for determining intrinsic mechanical properties of porous engineering ceramics and provides a predictive design tool for 3D-printed architected PDC-based metamaterials, with broad implications for multifunctional ceramic materials/structures across mechanical, thermal, and chemical applications.

Author contributions

Conceptualization: A. H. A., B. A., J. G., H. Y. S.; data curation: Y. L., H. M., Z. Y., and E. E.; formal analysis: Y. L.; funding acquisition: A. H. A., B. A., and J. G.; investigation: Y. L., V. K., H. Y. S., and M. J.; methodology: Y. L.; project administration: B. A., J. G., and A. H. A.; resources: A. H. A. and J. G.; supervision: A. H. A. and J. G.; visualization: Y. L. and A. H. A.; writing – original draft: Y. L. and H. Y. S.; writing – review & editing: All authors.

Conflicts of interest

The authors declare that they have no known competing financial interests or personal relationships that could have appeared to influence the work reported in this paper.

Data availability

The data supporting this article have been included as part of the supplementary information (SI). See DOI: https://doi.org/10.1039/d6mh00166a.

Acknowledgements

A. H. Akbarzadeh, H. Yazdani Sarvestani, J. Gholipour, and B. Ashrafi acknowledge the financial support of the National Research Council Canada. A. H. Akbarzadeh also acknowledges support from the Canada Research Chairs Program in Programmable Multifunctional Metamaterials, the Natural

Sciences and Engineering Research Council of Canada through an NSERC Discovery Grant (RGPIN-2022-04493), and the Canada Foundation for Innovation (CFI) through the John R. Evans Leaders Fund. The authors further acknowledge the assistance of Chakavak Nojavan, Ehsan Azad, and Apoorv Kulkarni (NRC) for their support with the 3D printing and pyrolysis processes, Dr Yongjun Xiao (McGill University) for his guidance on micro-CT scans, Xavier Pelletier (NRC) for his support on the operation of gas pycnometer, and Maxime Guérin (NRC) for his contributions in mechanical experiments. The authors gratefully acknowledge the guidance and assistance of Prof. Anja Geitmann and Dr Youssef Chebli, as well as the support of the Multi-scale Imaging Facility at McGill University, Macdonald Campus (Sainte-Anne-de-Bellevue, Québec, Canada), for SEM image acquisition. The authors would like to express their appreciation to Dr Hatem Titi (Department of Chemistry, McGill University) for his significant contribution to the X-ray diffraction (XRD) analysis. Language refinements were performed by ChatGPT.

References

1 H. Yazdani Sarvestani, V. Karamzadeh, A. Kulkarni, A. Sohrabi-Kashani, T. Lacelle, M. B. Jakubinek and B. Ashrafi, *Adv. Sci.*, 2025, **12**, 2416176.
2 H. Yazdani Sarvestani, T. Lacelle, A. Sohrabi-Kashani, A. Shashoua, V. Karamzadeh, H. Ravanbakhsh, A. Robitaille, H. Lavoie, C. Paquet, M. B. Jakubinek and B. Ashrafi, *Appl. Mater. Today*, 2024, **39**, 102327.
3 A. Sohrabi-Kashani, H. Yazdani Sarvestani, T. Lacelle, Y. Martinez-Rubi, S. Zou, A. Robitaille, H. Lavoie, M. B. Jakubinek and B. Ashrafi, *Composites, Part B*, 2025, **308**, 112991.
4 T. Lacelle, K. L. Sampson, H. Yazdani Sarvestani, A. Rahimizadeh, J. Barroeta Robles, M. Mirkhalaf, M. Rafiee, M. B. Jakubinek, C. Paquet and B. Ashrafi, *APL Mater.*, 2023, **11**(7), DOI: 10.1063/5.0151661.
5 V. Karamzadeh, H. Yazdani Sarvestani, A. Sohrabi-Kashani, A. Kulkarni, A. Jafari, T. Lacelle, H. Savoji, M. B. Jakubinek and B. Ashrafi, *Adv. Compos. Hybrid Mater.*, 2025, **8**, 223.
6 E. Ionescu, H. J. Kleebe and R. Riedel, *Chem. Soc. Rev.*, 2012, **41**, 5032–5052.
7 C. Vakifahmetoglu, D. Zeydanli and P. Colombo, *Mater. Sci. Eng., R*, 2016, **106**, 1–30.
8 Z. C. Eckel, C. Zhou, J. H. Martin, A. J. Jacobsen, W. B. Carter and T. A. Schaedler, *Science*, 2016, **351**, 58–62.
9 S. Walter, D. Suttor, T. Erny, B. Hahn and P. Greil, *J. Eur. Ceram. Soc.*, 1996, **16**, 387–393.
10 P. Cromme, M. Scheffler and P. Greil, *Adv. Eng. Mater.*, 2002, **4**, 873–877.
11 G. Perale, C. Giordano, F. Daniele, M. Masi, P. Colombo, L. Gottardo and S. Maccagnan, *Int. J. Appl. Ceram. Technol.*, 2008, **5**, 37–43.
12 C. Vakifahmetoglu, M. Buldu, A. Karakuscu, A. Ponzoni, D. Assefa and G. D. Soraru, *J. Eur. Ceram. Soc.*, 2015, **35**, 4447–4452.
13 R. O. Ritchie, *Nat. Mater.*, 2011, **10**, 817–822.
14 L. Brigo, J. E. M. Schmidt, A. Gandin, N. Michieli, P. Colombo and G. Brusatin, *Adv. Sci.*, 2018, **5**, 1800937.
15 A. R. Studart, U. T. Gonzenbach, E. Tervoort and L. J. Gauckler, *J. Am. Ceram. Soc.*, 2006, **89**, 1771–1789.
16 P. Colombo and J. R. Hellmann, *Mater. Res. Innovations*, 2016, **6**, 260–272.
17 Y. Liu, Y. Feng, H. Gong, Y. Zhang, X. Lin, B. Xie and J. Mao, *Ceram. Int.*, 2018, **44**, 10945–10950.
18 L. R. Meza, S. Das and J. R. Greer, *Science*, 2014, **345**, 1322–1326.
19 J. Shi, K. Ju, H. Chen, A. Mirabolghasemi, S. Akhtar, A. Sasmito and A. Akbarzadeh, *Nano Energy*, 2024, **123**, 109385.
20 J. Shi, K. Ju, H. Chen, V. Orsat, A. P. Sasmito, A. Ahmadi and A. Akbarzadeh, *Adv. Funct. Mater.*, 2024, **35**, 2417618.
21 J. Bauer, C. Crook, A. Guell Izard, Z. C. Eckel, N. Ruvalcaba, T. A. Schaedler and L. Valdevit, *Matter*, 2019, **1**, 1547–1556.
22 C. Moysan, R. Riedel, R. Harshe, T. Rouxel and F. Augereau, *J. Eur. Ceram. Soc.*, 2007, **27**, 397–403.
23 Z. Li, Z. Chen, J. Liu, Y. Fu, C. Liu, P. Wang, M. Jiang and C. Lao, *Virtual Phys. Prototyping*, 2020, **15**, 163–177.
24 L. Porz, A. J. Klomp, X. Fang, N. Li, C. Yildirim, C. Detlefs, E. Bruder, M. Hofling, W. Rheinheimer, E. A. Patterson, P. Gao, K. Durst, A. Nakamura, K. Albe, H. Simons and J. Rodel, *Mater. Horiz.*, 2021, **8**, 1528–1537.
25 K. Balazsi, D. Varanasi, Z. E. Horvath, M. Furko, F. S. Cinar and C. Balazsi, *Sci. Rep.*, 2022, **12**, 8250.
26 D. R. Smith, J. B. Pendry and M. C. Wiltshire, *Science*, 2004, **305**, 788–792.
27 H. Mofatteh, B. Shahryari, A. Mirabolghasemi, A. Seyedkanani, R. Shirzadkhani, G. Desharnais and A. Akbarzadeh, *Adv. Sci.*, 2022, **9**, e2202883.
28 J. Shi, H. Mofatteh, A. Mirabolghasemi, G. Desharnais and A. Akbarzadeh, *Adv. Mater.*, 2021, e2102423, DOI: 10.1002/adma.202102423.
29 T. Li and Y. Li, *Adv. Mater.*, 2024, e2309604, DOI: 10.1002/adma.202309604.
30 A. Rose, Z. Zhu, C. F. Madigan, T. M. Swager and V. Bulovic, *Nature*, 2005, **434**, 876–879.
31 Y. Chen, J. Cai, A. Seyedkanani, A. Akbarzadeh and M. Cerruti, *Mater. Horiz.*, 2026, **13**, 1350–1361.
32 H. Yazdani Sarvestani, D. Aranguren van Egmond, I. Esmail, M. Genest, C. Paquet and B. Ashrafi, *Adv. Funct. Mater.*, 2021, **32**, 2108492.
33 J. Cai, A. Seyedkanani, B. Shahryari, Z. Yan, P.-X. Lu, V. Orsat and A. Akbarzadeh Shafaroudi, *Mater. Horiz.*, 2026, **13**, 2830–2843.
34 A. A. Zadpoor, *Mater. Horiz.*, 2016, **3**, 371–381.
35 T. A. Schaedler, A. J. Jacobsen, A. Torrents, A. E. Sorensen, J. Lian, J. R. Greer, L. Valdevit and W. B. Carter, *Science*, 2011, **334**, 962–965.
36 M. C. Fernandes, J. Aizenberg, J. C. Weaver and K. Bertoldi, *Nat. Mater.*, 2021, **20**, 237–241.

37 L. R. Meza, A. J. Zelhofer, N. Clarke, A. J. Mateos, D. M. Kochmann and J. R. Greer, *Proc. Natl. Acad. Sci. U. S. A.*, 2015, **112**, 11502–11507.
38 C. Crook, J. Bauer, A. Guell Izard, C. Santos de Oliveira, E. S. J. Martins de Souza, J. B. Berger and L. Valdevit, *Nat. Commun.*, 2020, **11**, 1579.
39 T. Tancogne-Dejean, M. Diamantopoulou, M. B. Gorji, C. Bonatti and D. Mohr, *Adv. Mater.*, 2018, **30**, e1803334.
40 I. J. G. A. M. F. Ashby, *Proc. R. Soc. London, Ser. A*, 1997, **382**, 43–59.
41 Y. Li, T. Gancheva, E. Estakhrianhaghighi, B. D. Favis and A. Akbarzadeh, *Addit. Manuf.*, 2023, **77**, 103805.
42 L. G. Blok, M. L. Longana, H. Yu and B. K. S. Woods, *Addit. Manuf.*, 2018, **22**, 176–186.
43 B. G. Compton and J. A. Lewis, *Adv. Mater.*, 2014, **26**, 5930–5935.
44 S. Hong, D. Sycks, H. F. Chan, S. Lin, G. P. Lopez, F. Guilak, K. W. Leong and X. Zhao, *Adv. Mater.*, 2015, **27**, 4035–4040.
45 R. L. Truby and J. A. Lewis, *Nature*, 2016, **540**, 371–378.
46 S. Yin, W. Guo, H. Wang, Y. Huang, R. Yang, Z. Hu, D. Chen, J. Xu and R. O. Ritchie, *J. Mech. Phys. Solids*, 2021, **149**, 104341.
47 A. Velasco-Hogan, J. Xu and M. A. Meyers, *Adv. Mater.*, 2018, **30**, e1800940.
48 N. R. Brodnik, J. Schmidt, P. Colombo and K. T. Faber, *Addit. Manuf.*, 2020, **31**, 100957.
49 J. M. Hundley, Z. C. Eckel, E. Schueller, K. Cante, S. M. Biesboer, B. D. Yahata and T. A. Schaedler, *Addit. Manuf.*, 2017, **18**, 95–102.
50 X. Wang, F. Schmidt, D. Hanaor, P. H. Kamm, S. Li and A. Gurlo, *Addit. Manuf.*, 2019, **27**, 80–90.
51 K. Huang, H. Elsayed, G. Franchin and P. Colombo, *Addit. Manuf.*, 2020, **33**, 101144.
52 J. J. Moyano, J. Mosa, M. Aparicio, D. Pérez-Coll, M. Belmonte, P. Miranzo and M. I. Osendi, *Addit. Manuf.*, 2019, **30**, 100849.
53 A. Zocca, C. M. Gomes, A. Staude, E. Bernardo, J. Günster and P. Colombo, *J. Mater. Res.*, 2013, **28**, 2243–2252.
54 Z. Ding, H. Zreiqat and M. Mirkhalaf, *Mater. Horiz.*, 2022, **9**, 2762–2772.
55 X. Cao, Y. Jiang, T. Zhao, P. Wang, Y. Wang, Z. Chen, Y. Li, D. Xiao and D. Fang, *Composites, Part B*, 2020, **194**, 108030.
56 B. Lozanovski, M. Leary, P. Tran, D. Shidid, M. Qian, P. Choong and M. Brandt, *Mater. Des.*, 2019, **171**, 107671.
57 T. Tancogne-Dejean and D. Mohr, *Int. J. Solids Struct.*, 2018, **138**, 24–39.
58 M. Benedetti, A. du Plessis, R. O. Ritchie, M. Dallago, N. Razavi and F. Berto, *Mater. Sci. Eng., R*, 2021, **144**, 100606.
59 P. Colombo, G. Mera, R. Riedel and G. D. Sorarù, *J. Am. Ceram. Soc.*, 2010, **93**, 1805–1837.
60 R. Hill, *J. Mech. Phys. Solids*, 1963, **11**, 357–372.
61 S. Kari, H. Berger and U. Gabbert, *Comput. Mater. Sci.*, 2007, **39**, 198–204.
62 S. Guessasma and G. D. Valle, *J. Cell. Plast.*, 2009, **45**, 119–136.
63 M. Gologanu, J.-B. Leblond, G. Perrin and J. Devaux, *Int. J. Solids Struct.*, 2001, **38**, 5581–5594.
64 Z. Yan, A. Rahimizadeh, Y. Zhang, Y. Zhou and L. Lessard, *Compos. Struct.*, 2023, **320**, 117177.
65 E. Estakhrianhaghighi, A. Mirabolghasemi, J. Shi, L. Lessard and A. H. Akbarzadeh, *Composites, Part B*, 2022, **238**, 109894.
66 A. Rahimizadeh, J. Kalman, R. Henri, K. Fayazbakhsh and L. Lessard, *Materials*, 2019, **12**, 3929.
67 M. Hori and S. Nemat-Nasser, *Mech. Mater.*, 1999, **31**, 667–682.
68 S. L. Omairey, P. D. Dunning and S. Sriramula, *Eng. Comput.*, 2018, **35**, 567–577.
69 A. A. Griffith, *The theory of rupture, International congress for applied mechanics*, 1924.
70 E. Zanchetta, M. Cattaldo, G. Franchin, M. Schwentenwein, J. Homa, G. Brusatin and P. Colombo, *Adv. Mater.*, 2016, **28**, 370–376.

